ADVANCED OPTICAL MATERIALS
www.advopticalmat.de

Evidence of Optical Circular Dichroism in GaAs-Based Nanowires Partially Covered with Gold

Grigore Leahu, Emilija Petronijevic, Alessandro Belardini, Marco Centini, Concita Sibilia, Teemu Hakkarainen, Eero Koivusalo, Marcelo Rizzo Piton, Soile Suomalainen, and Mircea Guina*

Semiconductor nanostructures hybridized with metals have been known to offer new opportunities in nonlinear optics, plasmonics, lasing, biosensors; among them GaAs-based nanowires (NWs) hybridized with gold can offer new functionalities, as chiral sensing and light manipulation, as well as circular polarization sources. This study investigates GaAs–AlGaAs–GaAs NWs fabricated by self-catalyzed growth on Si substrates, and partially covered with gold, thus inducing the symmetry breaking and a potential chiral response. Three different samples are investigated, each of them with a different morphology, as the length and the overall diameter ranging from 4.6 to 5.19 μm and from 138 up to 165 nm, respectively. The samples are first characterized by measuring the absorption spectra by using a scattering-free photoacoustic (PA) technique. Then, the circular dichroism (CD) is investigated by measuring PA absorption for circularly polarized light under different incident angles at 532 and 980 nm. An efficient CD is found for proper configurations, and results are in good agreement with extrinsic chiral theory predictions and numerical simulations. It is therefore proven that these samples exhibit chiral behavior, and can be further optimized. Moreover, PA technique can be used as an extremely sensitive and efficient technique to characterize their "extrinsic" chirality.

1. Introduction

Nanostructures with broken symmetry put in interaction with circularly polarized light can mimic the chiral response present in important molecules and DNA. Engineering these structures thus paves the way for the important applications spreading from negative refraction,[1–3] chiral sensing[4,5] to production of optical field carrying out optical angular momentum for quantum information applications.[6] It has been shown that plasmonic nanostructures forming 1D[7] elements, 2D metasurfaces,[8–10] and 3D metamaterials[11] can exhibit linear chiral response due to their own, intrinsic chirality. Also semiconductor nanostructures can exhibit chiral features.[12–16] From the optical point of view, chiral structures possess the ability to rotate the plane of the polarization of electromagnetic waves (optical activity), and give rise to circular dichroism—i.e., the difference in the absorption of right- and left-handed circular polarized light.

Apart from 3D chiral objects, the possibility to obtain optical chirality, i.e., optical activity, with nonchiral elements was studied in the past,[17] but only recently reconsidered.[18,19] This phenomenon is obtained when the experimental configuration composed by both the nonchiral object and the optical incident field is nonsuperimposable on its mirror image.[20] This is called "extrinsic" chirality; in our previous works we have investigated this type of chirality in tilted golden nanowires by means of both linear (reflection and absorption) and nonlinear (second harmonic generation) measurements.[20–23]

III–V semiconductor nanowires (NWs) have been widely investigated since they exhibit good waveguiding properties thus offering a light manipulation at nanoscale. Coupling of the incident light to the discrete leaky waveguide modes above the bandgap in NWs leads to increased resonant absorption, thus paving the way for important applications such as energy harvesting, spectral selectivity, lasing, spin angular momentum generation, etc.[24–27] Metallic NWs have also been investigated for plasmonic laser applications[28–30] and possibility of surface plasmon polaritons excitation.[31] One step further is the partial covering of such NWs with gold: this can induce, along with the proper experiment setup, the symmetry breaking which leads to chiral response.

In this paper, for the first time to our knowledge, we report on a circular dichroism behavior from semiconductor hexagonal

Dr. G. Leahu, E. Petronijevic, Dr. A. Belardini, Dr. M. Centini, Prof. C. Sibilia
SBAI Department
Sapienza University of Rome
Via Antonio Scarpa 16, Rome 00161, Italy
E-mail: concita.sibilia@uniroma1.it
Dr. T. Hakkarainen, E. Koivusalo, M. Rizzo Piton, Dr. S. Suomalainen, Prof. M. Guina
Optoelectronics Research Centre
Tampere University of Technology
Korkeakoulunkatu 3, 33720 Tampere, Finland
M. Rizzo Piton
Departamento de Física
Universidade Federal de São Carlos
CP 676 São Carlos, SP, Brazil

DOI: 10.1002/adom.201601063

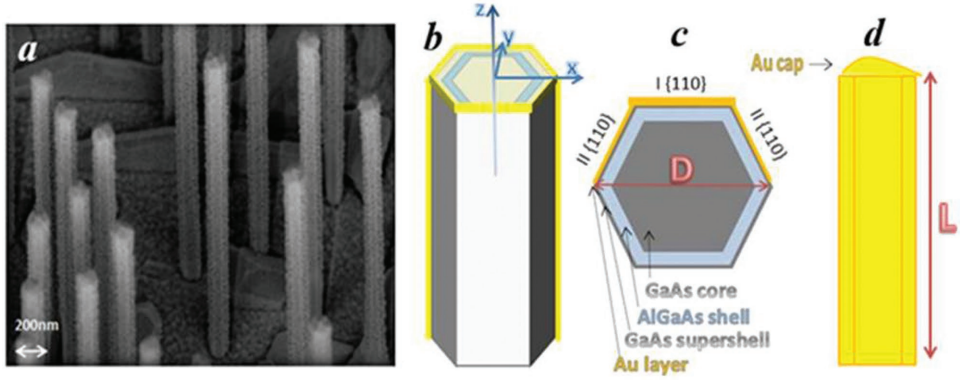

Figure 1. GaAs-based NWs partially covered with Au. a) Tilted (30°) SEM image of 3D distribution of S2. b) 3D schematic of the NW from the side not covered with Au (Au tip is made transparent to show GaAs–AlGaAs–GaAs configuration). c) *x*–*y* cross section with characteristic parameters: overall diameter *D*, which comprises GaAs core, AlGaAs shell, GaAs supershell. Au layer thickness on the sidewalls depends on the Au flux – the (110) sidewalls in the azimuthal flux direction (I{110}) are t_{gold_1} = 20 nm thick, while two other neighboring (110) facets (II{110}) are t_{gold_2} = 10 nm thick. d) *x*–*z* cross section from the Au-covered side. The Au cap is shaped depending on the direction of the flux, and its thickness varies from 20 to 40 nm.

nanowires partially covered by gold. The NWs were fabricated by means of molecular beam epitaxy on p-Si(111) using a lithography-free oxide patterning. This technique enables fabrication of highly uniform NW ensembles with tailorable NW density.[32] They were then exposed to a tilted flux of Au that resulted in nonuniform gold layers above the three sides and the tip of the NWs. The light that impinges on such structures under a proper oblique angle will be differently absorbed for circular polarizations of opposite handedness; this optical activity is usually indirectly measured as a difference in power transmitted/reflected by the chiral nanostructure-setup. More recently, we have shown that photoacoustic technique can be applied to directly measure circular dichroism in arrays of tilted gold NWs[23] as well as size-dependent resonant absorption properties of semiconductor NWs.[33] Here, we apply the same technique to investigate the "extrinsic" chirality in GaAs-based metal–semiconductor hybrid NWs under two wavelengths, 532 and 980 nm, corresponding to optical region of different light absorption by GaAs. Such composite material opens several interesting possibilities compared to metal NWs. The semiconductor NW not only acts as a waveguide and scaffolding for the metal structure but can also effectively convert photons to electron–hole-pairs and vice versa. This property is exploited in NW solar cells, photodetectors, and light-emitting diodes by incorporating a pn-junction within the NW. We believe that hybrid nanostructures combining the chiral optical response provided by the asymmetric metal and optoelectronic functionality of the semiconductor NWs can lead to nanophotonic applications in chiral sensing and light manipulation, as well as circular polarization sources.

2. Sample Fabrication

The coaxial GaAs–AlGaAs core–shell nanowires were grown by molecular beam epitaxy on p-Si(111) wafers using lithography-free Si/SiO_x patterns for defining the nucleation sites. The GaAs core was first grown by self-catalyzed growth mode. Then, the Ga catalyst droplet was consumed in As_2-flux in order to terminate axial growth. The $Al_{0.3}Ga_{0.7}As$ shell and GaAs supershell were then grown around the NW core using growth conditions that promote radial growth. The details of the Si/SiO_x pattern fabrication and NW growth are explained in details in ref. [24]. The NWs exhibit remarkably phase-pure zincblende crystal structure with the exception of short wurtzite segments formed at the tip of the NW during droplet crystallization when changing from axial to radial growth, see high-resolution transmission electron microscopy images and high-resolution X-ray diffraction spectra on similar samples in our recent paper.[34] The Au film was deposited on the NWs by electron beam evaporation. The incident angle of the Au-flux was 14° with respect to the NW axis. The NWs have hexagonal cross-section defined by (110)-facetted sidewalls. One of the (110) facetted NW sidewalls was selected as the azimuthal direction of the Au flux. The nominal Au thickness on this facet is t_{gold_1} = 20 nm, while on the neighboring (110) facets the Au thickness is t_{gold_2} = 10 nm due to flux geometry.

In **Figure 1**a, the tilted (30°) scanning electron microscopy (SEM) image of 3D distribution of one of the samples (S2 in **Table 1**) is shown. The 3D schematic and the *x*–*y* cross section are shown in Figure 1b,c, respectively. Characteristic geometric parameters are the NW length *L*, the overall diameter *D*, AlGaAs shell thickness t_{AlGaAs}, and GaAs supershell thickness t_{GaAs}. In Figure 1d, *x*–*z* cross section from the Au-covered side is shown. The Au cap is shaped depending on the direction of the flux, and its thickness varies from 20 to 40 nm. We test three samples having different lengths and diameters in order to experimentally

Table 1. Characteristic geometric parameters for the three samples together with their standard deviations. The samples exhibit low fabrication error margins.

Sample	*L* [nm]	*D* [nm]	t_{AlGaAs} [nm]	t_{GaAs} [nm]	t_{gold_1} [nm]	t_{gold_2} [nm]
S1	4750 ± 34	138 ± 5	3.5	0.7	20	10
S2	5190 ± 64	151 ± 5	8.6	1.7	20	10
S3	4600 ± 52	165 ± 6	11.7	5.8	20	10

evaluate the dependence of the CD signal to the geometrical parameters of the nanostructures and the fabrication tolerances (see Table 1 for geometrical data of the three samples—the Au evaporation parameters are equal for all the samples).

3. Photoacoustic Technique and Linear Characterization

We first experimentally characterize our samples by measuring their absorption by means of the photoacoustic (PA) technique. This technique is based on the generation of heat when a sample absorbs an incoming light beam. If the light intensity is modulated in time, a cycle of heating up and cooling down will correspond to changes in pressure that further produces an acoustic signal. The acoustic signal is then converted into electrical one by a sensitive microphone. This microphone is connected to the cell through a small tunnel, so that the scattered light cannot significantly contribute to PA signal, as shown in the inset of **Figure 2**a. Therefore, PA technique directly measures scattering independent absorption in the samples. It has been widely applied to characterize plasmonic nanoparticles and metasurfaces.[35–39]

We recently applied this technique to measure the resonant absorption in the NW samples of same geometric parameters before they had been exposed to Au flux.[33] Similar PA setup is shown in Figure 2a: the samples are shined from the air side by a Xenon arc lamp source followed by a monochromator, which provides the spectral range from 300 to 1100 nm. We show normal incidence absorption spectra for the samples S1–S3 in Figure 2b. The absorption maxima around 700–800 nm and 450–500 nm originate from HE_{11} and HE_{12} guided modes present in GaAs-based dielectric hexagonal NWs; however, due to the nonuniform Au layer and the interaction between close NWs, these maxima are significantly broadened. To simulate the absorption cross section of a single GaAs–AlGaAs–GaAs NW covered with Au we have used Lumerical finite difference time domain (FDTD). To take into account the interaction between the closely spaced NWs, we simulate two NWs whose distance is taken from the nearest neighbor statistics from top SEM images. The good agreement between numerical and PA spectra allows the assumption that the calculations will fit the PA experiments for circular incident light too.

4. Chiral Absorption Results

4.1. PA Circular Dichroism Setup

Since Au does not uniformly and symmetrically cover the hexagonal NWs, under oblique incidence, these structures promise to exhibit chiral effects under proper configurations. Therefore, we change our PA setup in order to be able to scan polarization and incidence angles, **Figure 3**a. We use two laser wavelengths: 532 nm to report on the range where all of the NW materials and Au strongly absorb energy, and 980 nm, where

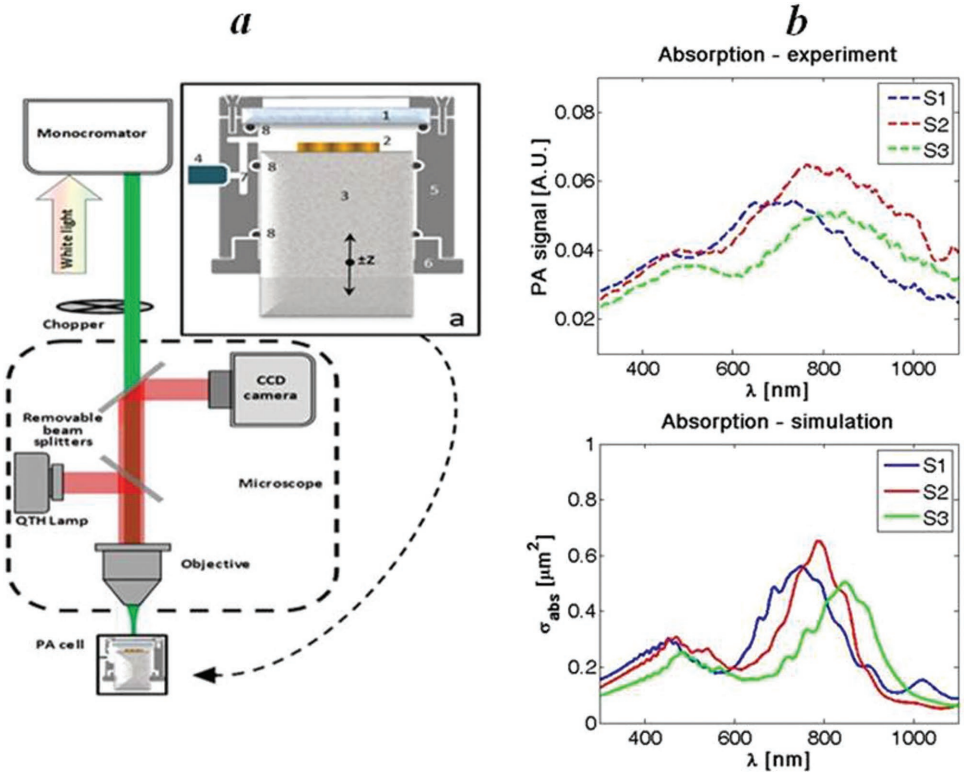

Figure 2. a) Experimental setup of the photoacoustic measurement. Inset (a): Variable volume photoacoustic cell, 1-quartz window, 2-sample, 3-quartz cylinder, 4-microphone, 5-inox cell body, 6-threaded flange, 7-sound labyrinth, 8-O-ring. b) PA spectra (dashed lines) and simulated absorption cross section (solid lines) of the three samples (S1 blue curves, S2 red curves, S3 green curves).

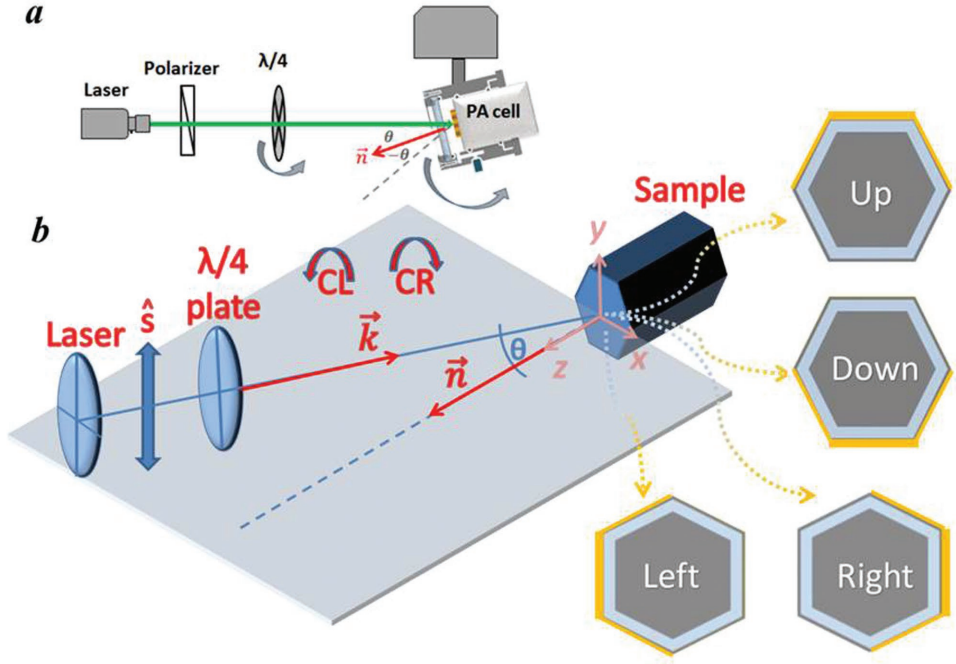

Figure 3. a) Top view of the circular dichroism measurements setup. Laser light at the wavelength of 532 or 980 nm is polarized so that it impinges with $\hat{s}$ polarization on a quarter wave plate. Rotational stage allows for the incident angle scan. b) 3D view of the experiment with four x–y plane configurations when primary I{110} sidewall is in: y_+ region – Up, y_- – Down, x_+ – Right, and x_- – Left.

GaAs and AlGaAs are almost nonabsorbing, while Au strongly reflects light (Si substrate is the only material that absorbs at 980 nm). The laser light is polarized before the quarter wave plate, so that it is $\hat{s}$-polarized when the fast wave plate's axis is at 0°. Fast axis wave plate scans the angles from −180° to 180°, where −45° represents left-handed circular polarization (CL) and 45° represents right-handed circular polarization (CR). PA cell is mounted on a rotational stage, which enables the incidence angle scan from $\theta = -56°$ to 56°, as well as four different NW configurations (see Figure 3b); NW primary sidewall covered with Au can be in xz plane toward y_+ direction (Up configuration), xz plane toward y_- direction (Down configuration), yz plane toward x_+ direction (Right configuration), and yz plane toward x_- direction (Left configuration).

4.2. CD Dependence on the Incidence Angle

As a figure of merit that defines the level of circular dichroism in PA measurements, we use

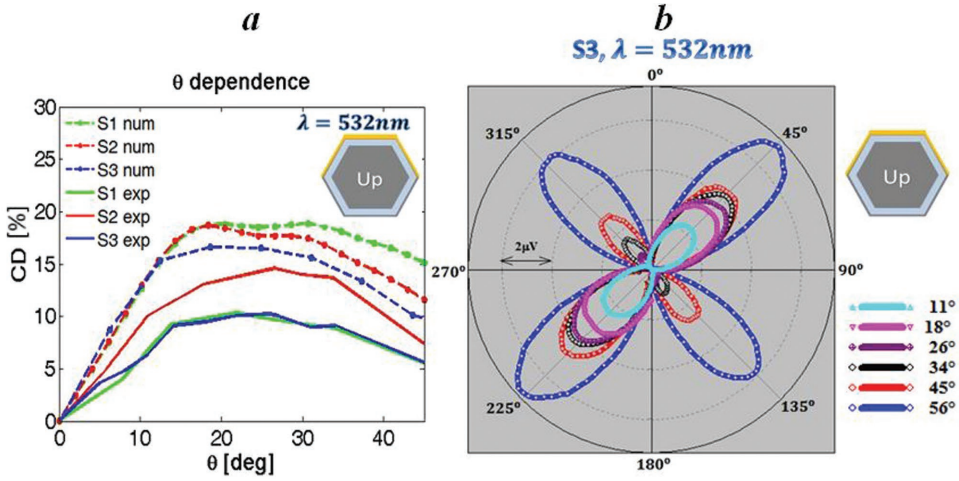

Figure 4. a) CD incidence angle dependence (experimental measured values in solid lines, numerical values in dashed lines) for the samples S1–S3 for the Up configuration at 532 nm; Sample S1 in green, S2 in red, S3 in blue. b) PA polar plots for S3 at 532 nm in Up configuration for various angles of incidence: 11° cyan, 18° magenta, 26° violet, 34° black, 45° red, 56° blue.

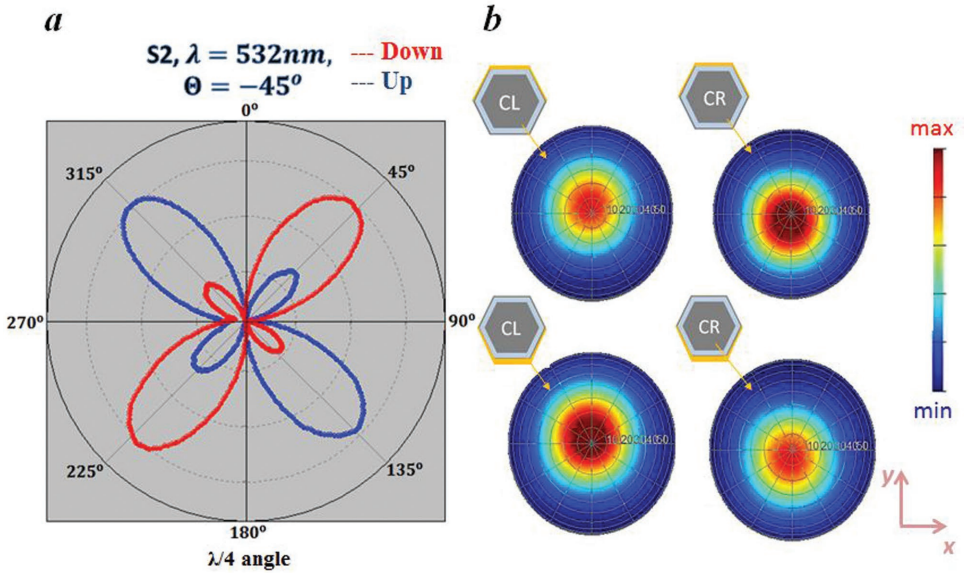

Figure 5. a) Polar plots of PA signal for Up (blue curve) and Down (red curve) configurations of S2 at 532 nm and −45° incidence. CD switches sign between the two configurations. b) Reflection far field intensity at 45° incidence for CL and CR impinging light in Up and Down configurations; we see that changing the input polarization from CL to CR we can control the reflected field intensity and direction (the centers of the plots indicate the specular reflection).

$$\mathrm{CD}[\%] = \frac{A_{\mathrm{CL}} - A_{\mathrm{CR}}}{A_{\mathrm{CL}} + A_{\mathrm{CR}}} \times 100 \quad (1)$$

where A_{CL} (A_{CR}) stands for the PA signal amplitude for CL (CR) polarization. In **Figure 4**a, we show measured (solid lines) and calculated (dashed lines) CD as a function of the incident angle for the three samples at 532 nm in Up configuration. We see that in all three samples CD increases from 0% at normal incidence, since both the setup and the structure are symmetric; in both Left and Right configurations, as well as for NWs samples without the asymmetric gold cover, CD is negligible, as the circularly polarized light does not see the symmetry breaking. CD

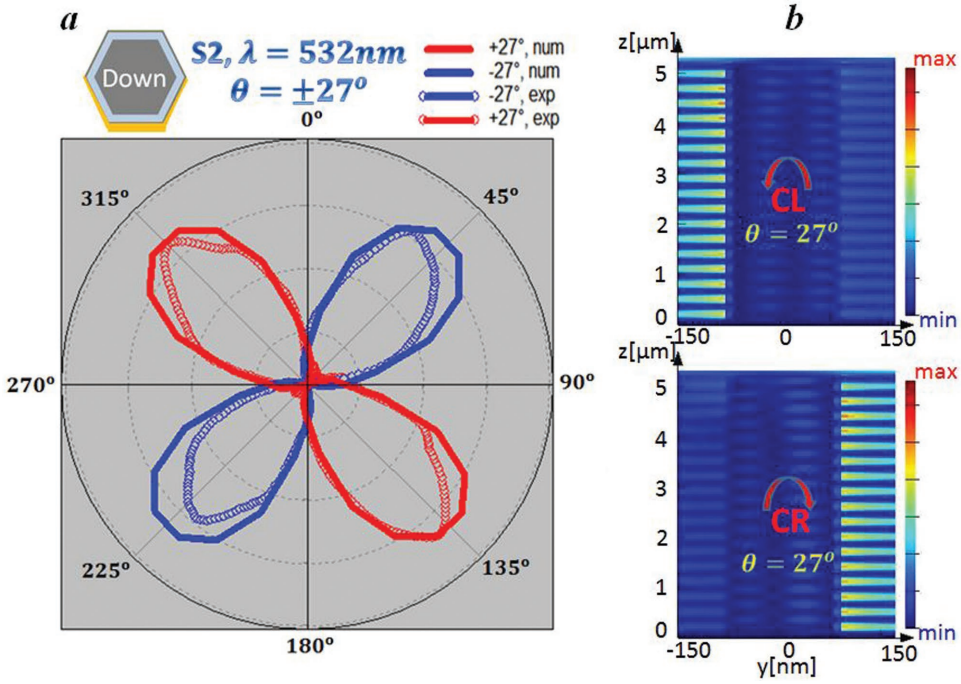

Figure 6. a) Polar plots (experimental values in open circles and numerical ones in solid lines) for Down configurations of S2 at 532 nm for −27° (blue) and 27° (red) incidence. CD has a 90° shift between these two configurations. b) Intensity of the electric field in *y*–*z* cross section when S2 is excited with CR or CL at 27°.

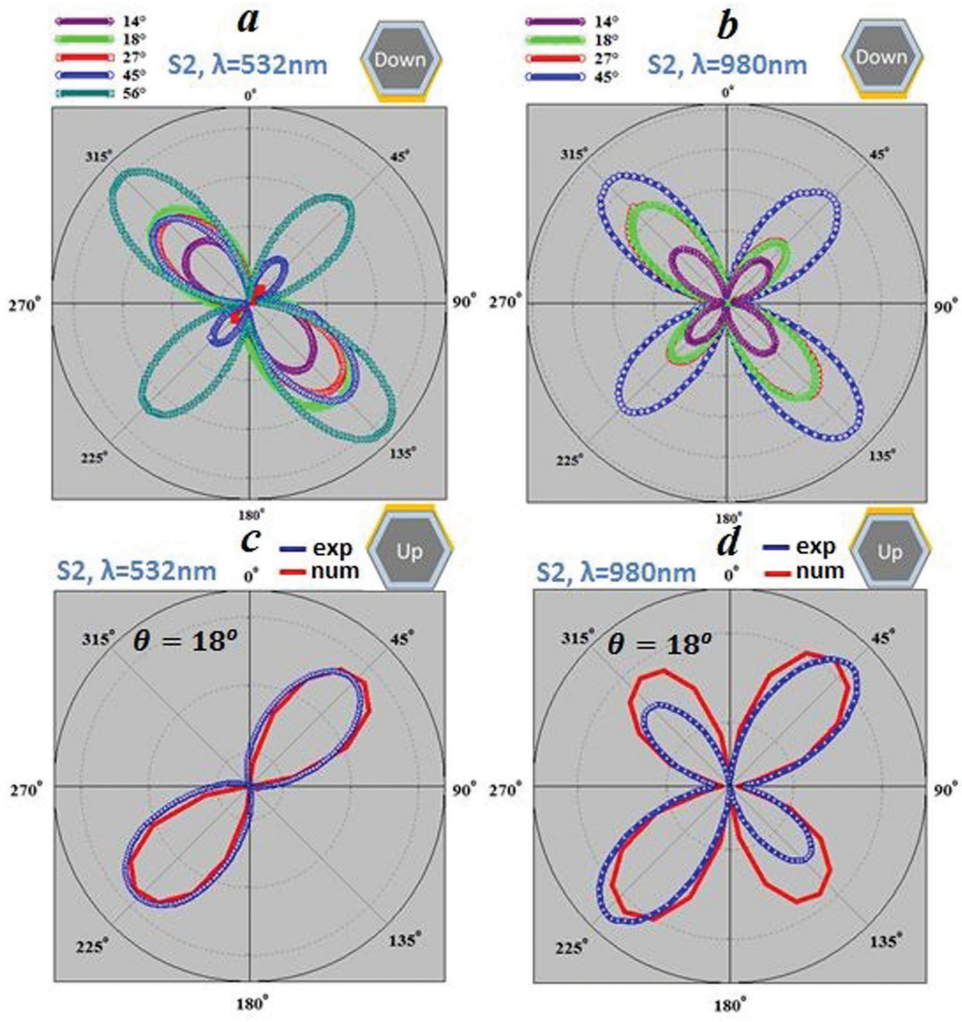

Figure 7. a) Polar plots of the PA signal obtained on sample S2 in Down configuration for different incidence angles at the wavelength of 532 nm. b) Polar plots of the PA signal obtained on sample S2 in Down configuration for different incidence angles at the wavelength of 980 nm. c) Numerical (red curve) and experimental (blue curve) PA signal for sample S2 at 18° of incidence at 532 nm in Up configuration. d) Numerical (red curve) and experimental (blue curve) PA signal are shown for sample S2 at 18° of incidence at 980 nm in Up configuration.

follows the form of the numerically calculated dependence, and the experimental maximum CD of 8% is reached for S2 at 27°; this sample has the longest L, while S1 and S3 have similar shorter L, which leads to a smaller CD. Thus, the results of the measurements in Figure 4a indicate that the dominant parameter in CD signal is attributed to the length of NWs, while the diameter does not have a strong influence on the chiral response. On the contrary, the diameter strongly affects the linear response of gold-free NWs.[33] However, PA signal has also a high contribution of a nonchiral Si substrate, while the simulations take into account just its small depth (limited by the calculation region), thus slightly overestimating CD. We attribute the other discrepancies to the fact that single NW simulations cannot completely catch the collective behavior due to the NW interactions and to the variations of fabrication parameters such as Au cap thickness. In Figure 4b, the polar plot of the PA signal is shown for S3 at 532 nm in Up configuration (0° corresponds to $\hat{s}$-polarized light) for different input angles of the impinging light. The difference between the lobes corresponding to CL and CR is strong at 11°, 18°, and 26°, while from 34° this difference decreases. Similar plots have been obtained for S1 and S2 samples.

Since sample S2 gives rise to the higher CD signal, in what follows we perform more detailed measurements on S2 by looking at different experimental geometries.

4.3. CD for Up and Down Configurations

In **Figure 5**a, we present polar plots of PA signals for the angle of incidence $\theta = -45°$, at 532 nm, for Down (red curve) and Up (blue curve) configurations. As expected from the theory of "extrinsic" chirality, the circular dichroism reverses its sign passing from Up to Down configuration. This influences also on the shape of the electromagnetic field reflected from the structure. In Figure 5b, we show the calculated reflection far field intensity at $\theta = 45°$ incidence for CL and CR illumination in Up and Down configurations. Both direction and intensity

of the reflected light change in these four combinations with respect the specular reflection direction, which indicates as possible applications of such NWs, the control the direction and intensity of the light.

4.4. Maximum CD at Opposite Incidence Angles

In **Figure 6**a, we show PA polar plot for the Down configuration, in the conditions where the maximum CD is achieved which is obtained for the sample S2 at around $\theta = 27°$ at 532 nm (see Figure 4a). As expected, the chiral feature shows 90° shift in polarization for the incidence angle of $\theta = -27°$. The "extrinsic" chirality is strong and we see no additional lobes.

It is also interesting to evaluate the field profile in the NW when the CD occurs. In Figure 6b, the simulations of the electric field intensity are shown if S2 is excited under $\theta = 27°$ at 532 nm wavelength. For CR the field is concentrated on the gold-covered sidewalls, while for CL it is concentrated on the opposite side. This suggests that these NWs could provide light path and polarization control. In particular, they could enable a completely new approach for chiral sensing in the form of hot electron Schottky photodetector[40] exploiting the circular polarization dependent plasmonic absorption at GaAs–Au interface.

4.5. Maximum CD at Different Wavelengths

We further examine the behavior at two different wavelengths: 532 and 980 nm. Since at 532 nm both Au and NW materials contribute to the absorption, while at 980 nm NWs are transparent and Au strongly reflects light, we expect CD to be significantly greater at 532 nm.

Indeed, angular dependence, gave CD values 50% lower at 980 nm with respect to 532 nm. In **Figure 7**, we report the comparison among the polar plots obtained at the above-mentioned wavelengths. In Figure 7a are shown the polar plots of the PA signal obtained on sample S2 in Down configuration for different incidence angles at the wavelength of 532 nm. In Figure 7b, we show the polar plots of the PA signal obtained in the same conditions at the wavelength of 980 nm. In Figure 7c, both numerical (red curve) and experimental (blue curve) PA signal are shown for sample S2 at $\theta = 18°$ of incidence at 532 nm in Up configuration; in Figure 7d, PA signal in the same condition at the wavelength of 980 nm is reported. We see that FDTD numerical simulations can efficiently predict the chiral behavior of these NW ensembles. This means that we can improve our fabrication parameters to optimize CD at wanted wavelengths, leading to unprecedented applications in chiral NW-based devices.

5. Conclusions

We experimentally investigate the effective chiral behavior of GaAs-based nanowire ensembles partially covered by gold. The employed fabrication process allows for the fabrication of highly uniform GaAs–AlGaAs NW ensembles; exposing them to the tilted Au flux leads to the asymmetric structure that exhibits CD behavior. The "extrinsic" chiral behavior was confirmed by measuring the differences in absorption of circular incident light of opposite handedness. Our scattering-independent PA setup directly measures the absorption and allows scanning of incidence angles and polarization. We have measured configurations with different symmetry and incidence angles, under two particular wavelengths, and numerically confirmed results by means of FDTD simulations. NW fabrication parameters can be further easily optimized to improve CD. By testing three samples having different dimensions, we infer that the NW diameter does not have a strong influence on the chiral response, while the length has a major effect; the strongest chiral response is observed for the longest NWs.

We strongly believe that bringing together the advantages of a semiconductor optoelectronics platform, waveguiding properties of vertical NWs, and chiral behavior when their symmetry is broken could lead to new perspectives in control of light at nanoscale and in developing new chiral sensing devices. To this end, our current efforts are dedicated to the development of prototype chiral photodetectors based on asymmetrically metal coated GaAs NWs including pn-junctions for collecting charge carriers.

Acknowledgements

The funding from the Academy of Finland Project NESP (decision number 294630) and NANoS (decision number 260815) is acknowledged.

Received: December 15, 2016
Revised: January 18, 2017
Published online:

[1] J. B. Pendry, *Science* **2004**, *306*, 1353.
[2] J. Zhou, J. Dong, B. Wang, T. Koschny, M. Kafesaki, C. M. Soukoulis, *Phys. Rev. B* **2009**, *79*, 121104 (R).
[3] S. Zhang, Y. Park, J. Li, X. Lu, W. Zhang, X. Zhang, *Phys. Rev. Lett.* **2009**, *102*, 023901.
[4] A. Kuzyk, R. Schreiber, Z. Fan, G. Pardatscher, E. Roller, A. Högele, F. C. Simmel, A. O. Govorov, T. Liedl, *Nature* **2012**, *483*, 311.
[5] Y. He, K. Lawrence, W. Ingram, Y. Zhao, *Chem. Commun.* **2016**, *52*, 2047.
[6] A. M. Yao, M. J. Padgett, *Adv. Opt. Photonics* **2007**, *446*, 3.
[7] H. K. Bisoyi, Q. Li, *Acc. Chem. Res.* **2014**, *47*, 3184.
[8] C. Wu, N. Arju, G. Kelp, J. A. Fan, J. Dominguez, E. Gonzales, E. Tutuc, I. Brener, G. Shvets, *Nat. Commun.* **2014**, *5*, 3892.
[9] V. K. Valev, J. J. Baumberg, B. De Clercq, N. Braz, X. Zheng, E. J. Osley, S. Vandendriessche, M. Hojeij, C. Blejean, J. Mertens, C. G. Biris, V. Volskiy, M. Ameloot, Y. Ekinci, G. A. E. Vandenbosch, P. A. Warburton, V. V. Moshchalkov, N. C. Panoiu, T. Verbiest, *Adv. Mater.* **2014**, *26*, 4074.
[10] V. K. Valev, J. J. Baumberg, C. Sibilia, T. Verbiest, *Adv. Mater.* **2013**, *25*, 2517.
[11] J. K. Gansel, M. Thiel, M. S. Rill, M. Decker, K. Bade, V. Saile, G. von Freymann, S. Linden, M. Wegener, *Science* **2009**, *325*, 1513.
[12] Y. Zhou, M. Yang, K. Sun, Z. Tang, N. A. Kotov, *J. Am. Chem. Soc.* **2010**, *132*, 6006.
[13] Y. Xia, Y. Zhou, Z. Tang, *Nanoscale* **2011**, *3*, 1375.

[14] Y. Zhou, Z. Zhu, W. Huang, W. Liu, S. Wu, X. Liu, Y. Gao, W. Zhang, Z. Tang, *Angew. Chem., Int. Ed.* **2011**, *50*, 11456.
[15] Y. Li, Y. Zhou, H. Y. Wang, S. Perrett, Y. Zhao, Z. Tang, G. Nie, *Angew. Chem., Int. Ed.* **2011**, *50*, 5860.
[16] Z. Zhu, J. Guo, W. Liu, Z. Li, B. Han, W. Zhang, Z. Tang, *Angew. Chem., Int. Ed.* **2013**, *52*, 13571.
[17] T. Verbiest, M. Kauranen, Y. van Rompaey, A. Persoons, *Phys. Rev. Lett.* **1996**, *77*, 1456.
[18] E. Plum, X.-X. Liu, V. A. Fedotov, Y. Chen, D. P. Tsai, N. I. Zheludev, *Phys. Rev. Lett.* **2009**, *102*, 113902.
[19] S. N. Volkov, K. Dolgaleva, R. W. Boyd, K. Jefimovs, J. Turunen, Y. Svirko, B. K. Canfield, M. Kauranen, *Phys. Rev. A* **2009**, *79*, 043819.
[20] M. Bertolotti, A. Belardini, A. Benedetti, C. Sibilia, *J. Opt. Soc. Am. B* **2015**, *32*, 1287.
[21] A. Belardini, M. C. Larciprete, M. Centini, E. Fazio, C. Sibilia, *Phys. Rev. Lett.* **2011**, *107*, 257401.
[22] A. Belardini, M. Centini, G. Leahu, E. Fazio, C. Sibilia, J. W. Haus, A. Sarangan, *Faraday Discuss.* **2015**, *178*, 357.
[23] A. Belardini, M. Centini, G. Leahu, D. C. Hooper, R. Li Voti, E. Fazio, J. W. Haus, A. Sarangan, V. K. Valev, C. Sibilia, *Sci. Rep.* **2016**, *6*, 31796.
[24] B. Mayer, D. Rudolph, J. Schnell, S. Morkötter, J. Winnerl, J. Treu, K. Müller, G. Bracher, G. Abstreiter, G. Koblmüller, J. J. Finley, *Nat. Commun.* **2013**, *4*, 2931.
[25] B. Mayer, L. Janker, B. Loitsch, J. Treu, T. Kostenbader, S. Lichtmannecker, T. Reichert, S. Morkötter, M. Kaniber, G. Abstreiter, C. Gies, G. Koblmüller, J. J. Finley, *Nano Lett.* **2016**, *16*, 152.
[26] S. Mokkapati, D. Saxena, H. H. Tan, C. J. Jagadish, *Sci. Rep.* **2015**, *5*, 15539.
[27] M. H. Alizadeh, B. M. Reinhard, *Opt. Express* **2016**, *24*, 8471.
[28] T. P. H. Sidiropoulos, R. Röder, S. Geburt, O. Hess, S. A. Maier, C. Ronning, R. F. Oulton, *Nat. Phys.* **2014**, *10*, 870.
[29] X. Wu, Y. Xiao, C. Meng, X. Zhang, S. Yu, Y. Wang, C. Yang, X. Guo, C. Z. Ning, L. Tong, *Nano Lett.* **2013**, *13*, 5654.
[30] R. F. Oulton, V. J. Sorger, T. Zentgraf, R. Ma, C. Gladden, L. Dai, G. Bartal, X. Zhang, *Nat. Lett.* **2009**, *461*, 629.
[31] S. Zhang, H. Wei, K. Bao, U. Håkanson, N. J. Halas, P. Nordlander, H. Xu, *Phys. Rev. Lett.* **2011**, *107*, 096801.
[32] T. V. Hakkarainen, A. Schramm, J. Mäkelä, P. Laukkanen, M. Guina, *Nanotechnology* **2015**, *26*, 275301.
[33] G. Leahu, E. Petronijevic, A. Belardini, M. Centini, R. Li Voti, T. Hakkarainen, E. Koivusalo, M. Guina, C. Sibilia, **2017**, unpublished.
[34] E. Koivusalo, T. Hakkarainen, M. Guina, **2017**, arXiv:1701.04264. arXiv.org e-Print archive. https://arxiv.org/abs/1701.04264 (accessed: February 2017).
[35] R. Inagaki, K. Kagami, E. T. Arakawa, *Phys. Rev. B* **1981**, *24*, 3644R.
[36] R. Inagaki, K. Kagami, E. T. Arakawa, *Appl. Opt.* **1982**, *21*, 949.
[37] T. El-Brolossy, T. Abdallah, M. Mohamed, S. Abdallah, K. Easawi, S. Negm, H. Talaat, *Eur. Phys. J.: Spec. Top.* **2008**, *153*, 361.
[38] R. Li Voti, G. Leahu, M. C. Larciprete, C. Sibilia, M. Bertolotti, I. Nefedov, I. V. Anoshkin, *Int. J. Thermophys.* **2015**, *36*, 1342.
[39] S. J. Zelewski, J. Kopaczek, W. M. Linhart, F. Ishikawa, S. Shimomura, R. Kudrawiec, *Appl. Phys. Lett.* **2016**, *109*, 182106.
[40] W. Li, J. G. Valentine, *Nanophotonics* **2017**, *6*, 177.